

Gate tunable enhancement of supercurrent in hybrid planar Josephson junctions

Peng Yu,¹ Han Fu,^{2,3} William F. Schiela,¹ William Strickland,¹ Bassel Heiba Elfeky,¹ S. M. Farzaneh,¹ Jacob Issokson,¹ Enrico Rossi,² and Javad Shabani¹

¹*Center for Quantum Information Physics, New York University, New York, NY 10003, USA*

²*Department of Physics, William & Mary, Williamsburg, Virginia 23187, USA*

³*Department of Physics, Florida Atlantic University, Boca Raton, Florida, 33431, USA*

(Dated: April 16, 2024)

Planar Josephson junctions (JJs) have emerged as a promising platform for the realization of topological superconductivity and Majorana zero modes. To obtain robust quasi one-dimensional (1D) topological superconducting states using planar JJs, limiting the number of 1D Andreev bound states' subbands that can be present, and increasing the size of the topological superconducting gap, are two fundamental challenges. It has been suggested that both problems can be addressed by properly designing the interfaces between the JJ's normal region and the superconducting leads. We fabricated Josephson junctions with periodic hole structures on the superconducting contact leads on InAs heterostructures with epitaxial superconducting Al. By depleting the chemical potential inside the hole region with a top gate, we observed an enhancement of the supercurrent across the junction. Such an enhancement is reproduced in theoretical simulations. The theoretical analysis shows that the enhancement of the JJ's critical current is achieved when the hole depletion is such to optimize the matching of quasiparticles' wave-function at the normal/superconductor interface. These results show how the combination of carefully designed patterns for the Al coverage, and external gates, can be successfully used to tune the density and wave functions' profiles in the normal region of the JJ, and therefore open a new avenue to tune some of the critical properties, such as number of subbands and size of the topological gap, that must be optimized to obtain robust quasi 1D superconducting states supporting Majorana bound states.

Planar Josephson junctions based on 2DEGs with spin-orbit coupling and induced superconductivity have attracted a lot of attention in recent years, mainly due to their potential to realize topological superconductivity and Majorana zero modes (MZM) [1–6]. Under the presence of a suitable Zeeman field, the normal region in the Josephson junction can serve as a quasi-one-dimensional channel, which can host Majorana zero modes at its ends [7, 8]. While solid progress has been made in both planar Josephson junctions and hybrid nanowire systems toward the realization of MZM [9–16], so far an unambiguous demonstration of MZM is still missing [17–20]. More and more evidence indicates that in hybrid systems there is a competition between disorder and the topological gap where disorder is still too strong [21, 22]. To make the hybrid system more robust against disorder, a large topological gap is preferable. As spin-orbit coupling and induced gaps jointly determine the size of the topological gap at finite magnetic fields [23], an ideal hybrid system should have strong spin-orbit coupling and a large induced gap. Such improvements are feasible with the development of new combinations of semiconductors and superconductors. For example, the recent introduction of Sn and Pb into the nanowire system brings a much larger induced gap [24, 25]. However, new materials also raise new challenges in material growth and device fabrication. InAs quantum well with epitaxial Aluminum, so far, is still the most suitable choice between nanofabrication and quality.

Compared to hybrid nanowire systems, planar Josephson junctions have a great advantage as the junction ge-

ometry can be easily modified to achieve strengthened properties. In particular, it might be possible to design the carrier density profiles and realize “wave-function” engineering using a combination of Al coverage patterns and external gates to minimize the number of subbands of Andreev bound states (ABSs), and maximize the topological superconducting gap. Several theoretical proposals also suggest modification of the Josephson junction geometry could lead to an enhanced induced gap and even an enhanced Rashba spin-orbit coupling [2, 26, 27]. With these potential benefits, it is natural to explore different geometries and utilize this degree of freedom to improve the system.

We fabricated Josephson junctions on epitaxial superconducting Al thin films grown in-situ on InAs heterostructures. Such devices have shown high transparency [28–31] a spin-orbit induced anomalous phase [32]. The junction is 4 μm long with a width of around 100 nm. Two rows of periodic holes are etched on each side of the Al contacts as shown in Fig. 1(a). Each hole is approximately 110 nm wide and 220 nm long. To control the chemical potential in the junction as well as in the hole region, we fabricated two layers of gates. In the first layer, a junction gate (JG) that covers the middle section of the junction is used to control the chemical potential in the junction. In the second layer, which is separated from the first layer of the gate by a second layer of dielectric, a top gate (TG) covers a much larger device region that includes the holes and the ends of the junction. A schematic diagram of the device and the material stacks are presented in Fig. 1(b). As shown in Fig. 1(a),

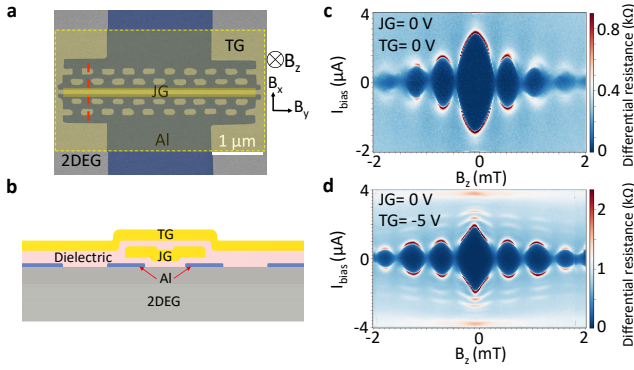


FIG. 1. Device geometry and Fraunhofer patterns at different gate configurations. (a) false-color scanning electron micrograph of the measured device. (b) of the device and the material stacks. (c)(d) Differential resistance as a function of the bias current and out-of-plane magnetic field for (c) $JG = 0$ V and $TG = 0$ V and (d) $JG = 0$ V and $TG = -5$ V.

the JG is shorter than the junction by 100 nm at each end by design. While JG itself cannot fully deplete the junction since it does not cover the ends of the junction, the chemical potential in the whole junction can still be fully controlled by using JG and TG together (Fig. S1). We notice TG depletes the ends of the junction around -2.5 V (Fig. S1). Since the 2DEG inside the hole region should have a similar density and coupling to TG as the 2DEG in the junction, we expect the 2DEG in the hole region should also be depleted around -2.5 V by TG. The depletion of the 2DEG in the hole region has a nontrivial effect on the junction, as discussed below. All the measurements in this study are performed in a dilution refrigerator equipped with a three-axis vector magnet. As shown in Fig. 1(a), the z-axis of the magnet is perpendicular to the device plane, while x and y-axes are in-plane fields aligned parallel and perpendicular to the current, respectively. Differential resistance is measured using standard low-frequency lock-in techniques in a four-point manner (more details about the device fabrication and measurement can be found in the methods section). In Fig. 1(c)(d), we present the differential resistance as a function of the bias current and applied out-of-plane magnetic field for two different gate configurations. To eliminate the hysteresis due to heating effects, the current bias is always swept from zero to high bias in these two scans. All gates are set to 0 for Fig. 1(c). For the results shown in Fig. 1(d), TG is set to -5 V while JG remains at 0. In Fig. 1(d), all the holes are supposed to be depleted as the result of a TG voltage below -2.3 V. In both configurations, the observed Fraunhofer patterns are symmetric with respect to the bias and the out-of-plane field, indicating an absence of hysteresis and a uniform supercurrent distribution across the junction. It is worth noting that extra resistance peaks have

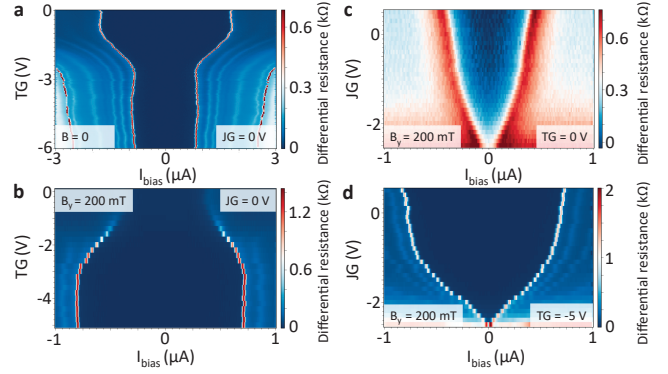


FIG. 2. Supercurrent gate dependence at different in-plane magnetic fields. (a) Differential resistance as a function of the bias current and TG voltages at zero magnetic field. (b) Differential resistance as a function of the bias current and TG voltages at $B_y = 200$ mT. The Supercurrent is significantly enhanced when more negative voltages is applied to TG. (c)(d) Differential resistance as a function of the bias current and JG voltages at $B_y = 200$ mT when $TG = 0$ V (c) and $TG = -5$ V (d). Depletion of holes (d) brings more supercurrent than when the holes are not depleted (c).

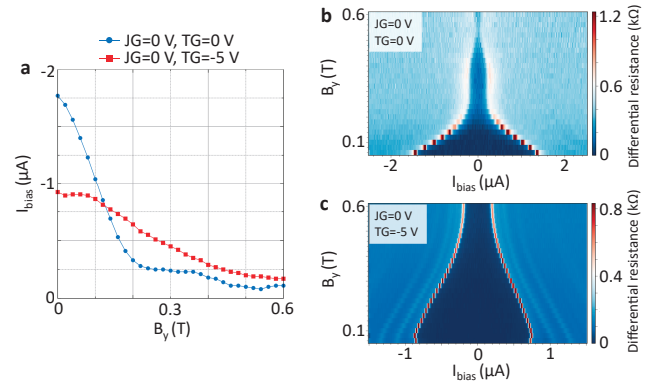


FIG. 3. Supercurrent in-plane field dependence at different gate configurations. (a) Switching current extracted from panels (b) and (c). (b) Differential resistance as a function of the bias current and B_y when $JG = 0$ V and $TG = 0$ V. (c) Differential resistance as a function of the bias current and B_y when $JG = 0$ V and $TG = -5$ V. When the holes are depleted (c), the supercurrent shows an almost linear decreasing with increasing B_y .

been observed in Fig. 1(d), which possibly indicates a stronger multiple Andreev reflection when the hole region is depleted. Overall, the two Fraunhofer patterns show similar periodicity, suggesting the effective junction area is not significantly modified by the depletion of the hole region. Next, we characterize the supercurrent gate dependence at different magnetic fields. At zero field, the supercurrent decreases when the voltage on TG is swept from 0 to -3 V as the result of the depletion of the ends

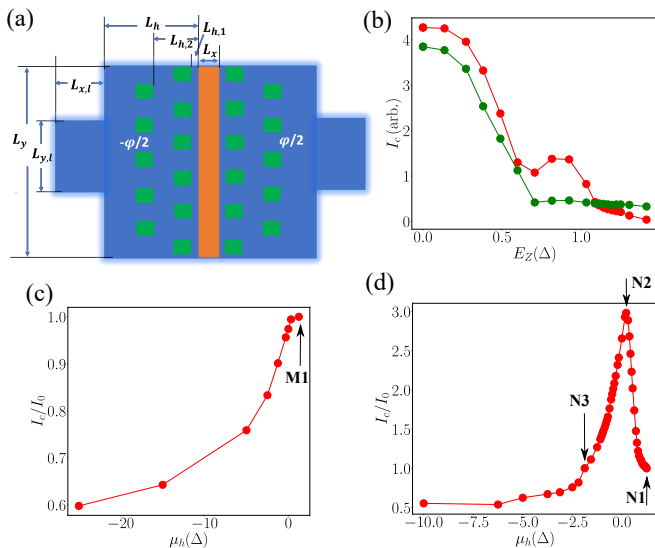


FIG. 4. (a) Schematic of simulation setup to model the experiments. (b) I_c as a function of E_Z for $\mu_h = \mu = 1.25\Delta$ (red) and $\mu_h = -1.25\Delta$ (green). (c), (d) I_c vs μ_h for $E_Z = 0$ and $E_Z = 1.14\Delta$, respectively. In (c) and (d) I_0 is the value of I_c when $\mu_h = \mu$.

of the junction (Fig. 2(a)). Below $TG = -3$ V, however, the supercurrent remains almost unchanged. For JG, the dependence is simpler as the supercurrent always monotonically decreases with decreasing JG voltages (Fig.s). When the magnetic field is turned on, the supercurrent shows a very different behavior. At $B_y = 200$ mT, where B_y is perpendicular to the supercurrent, the supercurrent is enhanced when more negative voltage is applied to the TG (Fig. 2(b)). The supercurrent reaches its maximum around $TG = -2.5$ V and remains constant after that. Applying a more negative voltage on TG can deplete both the ends of the junction and the hole region. Depletion of the ends of the junction should lead to a drop of the supercurrent as shown in Fig. 2(a). For fields parallel to the supercurrent, we also observed a similar enhancement of supercurrent with TG voltages (Fig.s). When TG is fixed to 0 V and -5 V and $B_y = 200$ mT, sweeping JG reveals that the supercurrent still monotonically decreases with decreasing JG voltages (Fig. 2(c)(d)). That indicates the enhancement of supercurrent is solely determined by the TG voltage and is not related to the change of chemical potential in the junction.

The enhancement of the supercurrent can also be observed in in-plane magnetic field scans when the gate voltages are fixed. In Fig. 3(b), we plot differential resistance as a function of B_y and bias current for $TG = 0$ V. The supercurrent exhibits a nonlinear behavior as it first quickly decreases at low fields followed by a much slower decline at higher fields. The supercurrent also shows some wiggles at higher fields. Overall, the supercurrent at $B_y = 0.5$ T is less than 10 percent of the supercurrent at $B_y = 0.1$ T. We notice the differ-

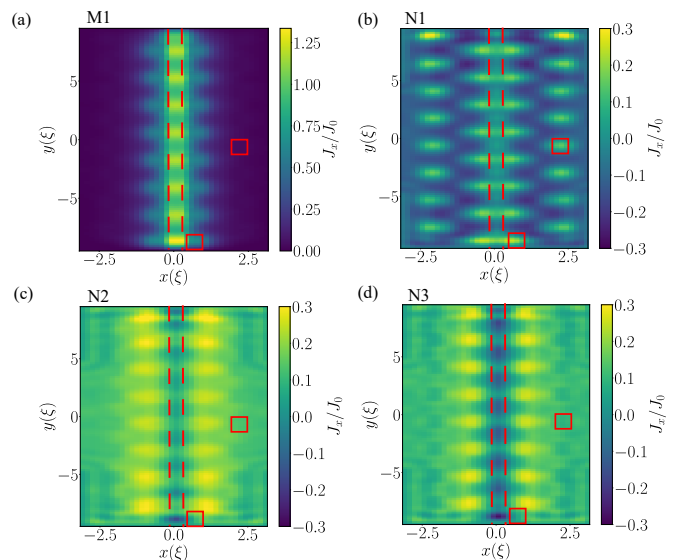


FIG. 5. Profile of J_x for the case when $E_Z = 0$ and $\mu_h = \mu$, M1 point in Fig. 4 (c). (b), (c), (d) Profiles of J_x for the case when $E_Z = 1.14\Delta$ and μ_h corresponds to the points N1, N2, N3 in Fig. 4 (d), respectively. J_0 is the average current density for the case when $E_Z = 0$, $\mu_h = \mu$. The red dashed lines indicate the boundary of the normal strip. The red boxes show positions of some of the depleted holes.

ential resistance of the "supercurrent" is finite at high fields, which is occasionally seen in our junctions. We attribute it to some part of the junction becoming normal at high fields. But the sudden dropping in resistance and the Fraunhofer patterns at high fields (Fig. S2) indicate there is still supercurrent flow through the semiconductor part of the junction. When TG is fixed to -5 V, Fig. 3(c), the supercurrent has an almost linear dependence on B_y . From $B_y = 0.1$ T $B_y B_x = 0.5$ T, the supercurrent still preserves 40 percent of its value and the resistance remains to zero. In Fig. 3(a), we extract the switching current from Fig. 3(b)(c) and plot them together. As can be seen, the two switching currents cross around $B_y = 0.12$ T, confirming the observation that the enhancement of the supercurrent only happens at finite fields and when the voltage on TG is below the specific value. In another device, we have observed a similar enhancement of supercurrent at finite fields when TG is below a certain value (see supplementary information for more details).

To understand the origin of this dependence of critical currents on the gate voltage, we setup a tight-binding model for the Bogoliubov de Gennes (BdG) Hamiltonian describing the system, see SM for details, using the python package Kwant [33]. To be able to obtain from the model all the desired quantities, in particular the critical current, with the available computational resources, we scaled down all the dimensions while using a value of the superconducting gap Δ and of the chemical potential μ in the regions outside the holes such that the

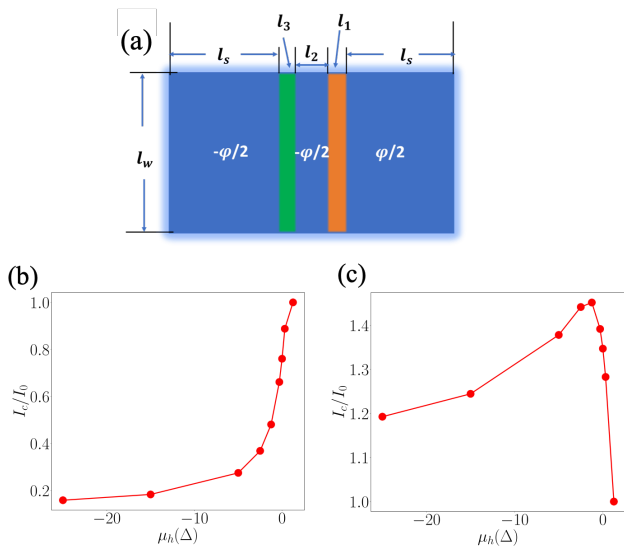


FIG. 6. (a) Layout of simplified two-strip model. (b) Scaling of I_c with μ_h obtained using the simplified model for the case when $l_2 = \xi/6$. (c) Same as (b) for the case when $l_2 = \xi/2$. In (b) and (c) $I_0 = I_c(\mu_h = \mu)$.

ratio between the geometric dimensions and the superconducting coherence length, ξ , is of the same order as in the experiment. For the results presented below we use a value of Δ 16 times larger than the physical one and set $\mu = 1.25\Delta$. The geometry of the model used is shown in Fig. 4 (a). To properly model the superconducting leads we chose a value of $L_{x,l}$, see Fig. 4 (a), sufficiently larger than ξ to avoid spurious finite-size effects.

We first obtain the ABSs's spectrum $\{\epsilon_n(\varphi)\}$ as a function of the phase difference φ between the superconducting pairing of the two leads. We then calculate the supercurrent $I(\varphi) = \sum_{\epsilon_n < 0} (\partial\epsilon_n/\partial\varphi)(2\pi/\Phi_0)$, where $\Phi_0 = h/2e$ is the magnetic flux quantum. From this, the critical current $I_c = \max(I(\varphi))$ is extracted for different values of the in-plane magnetic field and chemical potential μ_h of the holes.

Figure 4 (b) shows the evolution of I_c with the strength of the Zeeman energy E_Z due to an in-plane magnetic field perpendicular to the current for the case when $\mu_h = \mu$, in red, and $\mu_h = -1.25\Delta$, in green. The Zeeman energy in the superconductor is taken to be 1/2 the value in the normal and depleted regions. In the first case the holes are normal regions, i.e., regions where Δ is set to zero, with the same carrier density as the rest of the system. In the second case the carrier density in the holes is lower than in the areas around them. In both cases we see that I_c first decreases with E_Z up to $E_Z \approx 0.6\Delta$. For $E_Z > 0.6\Delta$ in the first case I_c changes non-monotonically with E_Z , a behavior that can be attributed to the almost closing a reopening of the gap of the ABS's spectrum. In the second case I_c keeps decreasing also for $E_Z > 0.6\Delta$, albeit more slowly, suggesting that in this case the gap

of the ABS doesn't recover with E_Z .

As in the experimental case, from Fig. 4 (b), we see that above a threshold value of E_Z , $E_Z \approx 1.1\Delta$, I_c for the depleted case is larger than for the non-depleted suggesting that for $E_Z > 1.1\Delta$ the evolution of I_c with μ_h might be not monotonic. This is confirmed by the results for the evolution of I_c with respect to μ_h shown in Fig. 4 (c), (d), for the $E_Z = 0$ and $E_Z = 1.14\Delta$ cases, respectively. We see that for $E_Z = 0$ I_c decreases monotonically as the depletion ($-\mu_h$) of the holes increases, whereas for $E_Z = 1.14\Delta$ I_c varies non-monotonically with μ_h , in qualitative agreement with the experimental results.

We have verified, see SM, that different values of the spin-orbit coupling (SOC) strength, and different directions of the in-plane magnetic field do not modify qualitatively the results presented in Fig. 4 (b)-(d).

Figure 5 shows the spatial profile of the quasiparticle current density $J_x(x, y) = -i(\hbar/2m^*) \sum_{\epsilon_n < 0} (\psi_n^* \nabla \psi_n - \psi_n \nabla \psi_n^*)$ [34], where ψ_n are the eigenstates of the BdG Hamiltonian. Notice that the regions where $J = 0$ are regions where the current is carried by the superconducting condensate. Panel (a) shows the profile of J for the case when $E_Z = 0$. We see that the presence of the holes induces a periodic modulation in the transverse direction of the current in the normal region of the JJ. Panels (b), (c), (d) show the results for the case $E_Z = 1.14\Delta$ for the values of μ_h denoted by $N1$, $N2$, and $N3$ in Fig. 4 (d). We see that for the value of μ_h for which I_c is maximum, panel (c), J is more uniform in the central region of the JJ. This suggests that the optimal value of μ_h results in a better matching of the quasiparticle wave-functions across the different regions of the JJ.

To check that this is the case we considered a simplified model, shown in Fig. 6 (a). In this model the holes are effectively replaced by a normal strip, shown in green in Fig. 6 (a), at a distance l_2 from the normal region of the JJ. Notice that the difference of the superconducting phase across the normal region modeling the holes is set to zero. This is done to take into account that in the experimental geometry there are paths between the holes that connect the different superconducting regions on the same side of the JJ's normal region, the region shown in orange in Fig. 6 (a), that separates the left and right superconducting leads.

Using the simplified model we were able to see that the critical parameter determining the nature of the evolution of I_c with respect to μ_h is the distance l_2 between the normal region modeling the holes, the depletion strip, and the JJ normal region. Figures 6 (b), (c), show the results for $l_2 = \xi/6$ and $l_2 = \xi/2$, respectively, when both E_Z and SOC are not present. The results show that when $l_2 \ll \xi$ I_c decreases monotonically with ($-\mu_h$), and that when $l_2 \sim \xi$ I_c varies non-monotonically with ($-\mu_h$). For $l_2 \gg \xi$ the two normal strips are effectively decoupled from each other and so μ_h has no effect on

I_c . These results suggest that the main reason why experimentally a non-monotonic scaling of I_c vs $(-\mu_h)$ is observed in the presence of an in-plane magnetic field is the fact that when $E_Z \gtrsim \Delta$ the ABSs' wave functions decay faster in the superconducting regions at the sides of the JJ's normal region, effect that in the simplified model corresponds to a reduction of ξ [35] and therefore to an increase of the ratio l_2/ξ to values ~ 1 for which I_c scales non-monotonically with μ_h .

To further understand the origin of the observed dependence of I_c on l_2/ξ and μ_h we calculated the reflection coefficients of a superconducting-normal (SN) junction with a depletion region on the superconducting side at a distance l_2 from the SN interface, see SM for details. We found that the ratio $|r_A/r_N|$ between Andreev reflection, r_A , and normal reflection, r_N , is strongly affected by μ_h when $l_2 = \xi/2$ due to the fact that in this case the amplitude of the electron wave function at the SN interface can be tuned in and out of the value that maximizes r_A by varying $(-\mu_h)$. We therefore conclude that varying via an external gate the depletion of the holes for a JJ like the one shown in Fig.1 (a) results in the effective tuning of the spatial profile of the quasiparticles wave functions leading to qualitative changes of critical properties such as the JJ's critical current.

In summary, we have fabricated Josephson junctions with periodic hole structures on the Al contact. A counter intuitive enhancement of supercurrent has been observed when the 2DEG in the hole region is depleted by the TG. Theoretical modeling and careful analysis of the experimental results show that such unusual enhancement of the critical current is due to changes of the spatial profile of the quasiparticles' wave functions. The ability to shape engineer the wave function of the electronic quantum states is critical to realize robust topological superconducting states supporting non-Abelian quasiparticles. Our results show that by combining specific Al coverage layouts in InAs/Al planar JJs with external gates a unique control of the profile of the electrons' wave functions can be achieved resulting in remarkable tunability of key properties of the JJs.

Methods

Wafers are grown by molecular beam epitaxy. Devices are fabricated using a combination of wet etching and deposition techniques after electron beam lithography. Device mesa features are defined by a deep wet etch with 85% concentrated phosphoric acid, 30% concentrated hydrogen peroxide, and deionized water in a volumetric ratio of 1:1:40 after selectively etching the aluminum top layer with Transene Aluminum Etchant Type D. Junction weak links and smaller device features are defined by a subsequent aluminum etch. Double-layer gates subsequently undergo two cycles of dielectric deposition of

aluminum oxide via atomic layer deposition, and titanium/gold gates are deposited via electron beam evaporation. Measurements are performed in a dilution refrigerator at a temperature of around 30 mK using standard low-frequency lock-in amplification techniques with excitation currents of at most 10 nA and frequencies of around 17 and 77 Hz. Magnetic field is generated by a three-axis superconducting vector magnet.

Author Contributions

W.M.S. grew the material heterostructure. P.Y. fabricated the devices. P.Y. with the help of W. F. S., B. H. E, S. M. F. performed the measurements. H.F. and E.R. developed the theoretical description and obtained the theoretical results. P.Y., H.F., E.R. and J.S. analyzed the results and wrote the manuscript with contributions from all of the authors.

Acknowledgements

Project was funded by the US Department of Energy, Office of Basic Energy Sciences, via Award DE-SC0022245. It was partially supported in part by DARPA Topological Excitations in Electronics (TEE) program under grant No. DP18AP900007, the U.S. Office of Naval Research (ONR) through Grants No. N000142112450 and MURI No. N000142212764. H.F. and E.R. thank Joseph J. Cuzzo for very helpful discussions during the initial stages of the work.

-
- [1] F. Setiawan, A. Stern, and E. Berg, Topological superconductivity in planar josephson junctions: Narrowing down to the nanowire limit, *Phys. Rev. B* **99**, 220506 (2019).
 - [2] A. Melo, S. Rubbert, and A. R. Akhmerov, Supercurrent-induced Majorana bound states in a planar geometry, *SciPost Phys.* **7**, 39 (2019).
 - [3] O. Lesser, A. Saydjari, M. Wesson, A. Yacoby, and Y. Oreg, Phase-induced topological superconductivity in a planar heterostructure, *Proceedings of the National Academy of Sciences of the United States of America* **118**(27), e2107377118 (2021).
 - [4] N. Mohanta, S. Okamoto, and E. Dagotto, Skyrmion control of majorana states in planar josephson junctions, *Communications Physics* **4**, 163 (2021).
 - [5] C. Peng, A. Haim, T. Karzig, Y. Peng, and G. Refael, Floquet Majorana bound states in voltage-biased planar Josephson junctions, *Physical Review Research* **3**, 023108 (2021).
 - [6] A. Banerjee, O. Lesser, M. A. Rahman, H.-R. Wang, M.-R. Li, A. Kringhøj, A. M. Whiticar, A. C. C. Drachmann, C. Thomas, T. Wang, M. J. Manfra, E. Berg, Y. Oreg, A. Stern, and C. M. Marcus, Signatures of a topological

- phase transition in a planar Josephson junction, *Phys. Rev. B* **107**, 245304 (2023).
- [7] M. Hell, M. Leijnse, and K. Flensberg, Two-dimensional platform for networks of Majorana bound states, *Phys. Rev. Lett.* **118**, 107701 (2017).
- [8] F. Pientka, A. Keselman, E. Berg, A. Yacoby, A. Stern, and B. I. Halperin, Topological superconductivity in a planar Josephson junction, *Phys. Rev. X* **7**, 021032 (2017), 1609.09482.
- [9] V. Mourik, K. Zuo, S. M. Frolov, S. R. Plissard, E. P. A. M. Bakkers, and L. P. Kouwenhoven, Signatures of Majorana fermions in hybrid superconductor-semiconductor nanowire devices, *Science* **336**, 1003 (2012).
- [10] M. T. Deng, S. Vaitiekenas, E. B. Hansen, J. Danon, M. Leijnse, K. Flensberg, J. Nygård, P. Krogstrup, and C. M. Marcus, Majorana bound state in a coupled quantum-dot hybrid-nanowire system, *Science* **354**, 1557 (2016).
- [11] J. Chen, P. Yu, J. Stenger, M. Hocevar, D. Car, S. R. Plissard, E. P. A. M. Bakkers, T. D. Stanescu, and S. M. Frolov, Experimental phase diagram of zero-bias conductance peaks in superconductor/semiconductor nanowire devices, *Science Advances* **3**, e1701476 (2017).
- [12] J. Shabani, M. Kjaergaard, H. J. Suominen, Y. Kim, F. Nichele, K. Pakrouski, T. Stankevic, R. M. Lutchyn, P. Krogstrup, R. Feidenhans'l, S. Kraemer, C. Nayak, M. Troyer, C. M. Marcus, and C. J. Palmstrøm, Two-dimensional epitaxial superconductor-semiconductor heterostructures: A platform for topological superconducting networks, *Phys. Rev. B* **93**, 155402 (2016).
- [13] H. Ren, F. Pientka, S. Hart, A. T. Pierce, M. Kosowsky, L. Lunzner, R. Schlereth, B. Scharf, E. M. Hankiewicz, L. W. Molenkamp, B. I. Halperin, and A. Yacoby, Topological superconductivity in a phase-controlled Josephson junction, *Nature* **569**, 93 (2019).
- [14] A. Fornieri, A. M. Whitticar, F. Setiawan, E. Portolés, A. C. C. Drachmann, A. Keselman, S. Gronin, C. Thomas, T. Wang, R. Kallahaer, G. C. Gardner, E. Berg, M. J. Manfra, A. Stern, C. M. Marcus, and F. Nichele, Evidence of topological superconductivity in planar Josephson junctions, *Nature* **569**, 89 (2019).
- [15] M. C. Dartiailh, W. Mayer, J. Yuan, K. S. Wickramasinghe, A. Matos-Abiague, I. Žutić, and J. Shabani, Phase signature of topological transition in Josephson junctions, *Phys. Rev. Lett.* **126**, 036802 (2021), 1906.01179.
- [16] D.-X. Qu, J. J. Cuzzo, N. E. Teslich, K. G. Ray, Z. Dai, T. T. Li, G. F. Chapline, J. L. DuBois, and E. Rossi, Phase-Slip Lines and Anomalous Josephson Effects in Tungsten Nanoscale Cluster-Based Topological Insulator Nanobridges: Implications for Topologically Protected Qubits and Quantum Sensors, *ACS Applied Nano Materials* **7**, 3702 (2024).
- [17] S. Das Sarma and H. Pan, Disorder-induced zero-bias peaks in Majorana nanowires, *Phys. Rev. B* **103**, 195158 (2021).
- [18] P. Yu, J. Chen, M. Gomanko, G. Badawy, E. P. A. M. Bakkers, K. Zuo, V. Mourik, and S. M. Frolov, Non-Majorana states yield nearly quantized conductance in proximatized nanowires, *Nature Physics* **10.1038/s41567-020-01107-w** (2021).
- [19] H. Pan and S. Das Sarma, Physical mechanisms for zero-bias conductance peaks in Majorana nanowires, *Phys. Rev. Research* **2**, 013377 (2020).
- [20] J. Chen, B. Woods, P. Yu, M. Hocevar, D. Car, S. Plissard, E. Bakkers, T. Stanescu, and S. Frolov, Ubiquitous Non-Majorana Zero-Bias Conductance Peaks in Nanowire Devices, *Physical Review Letters* **123**, 107703 (2019).
- [21] S. Ahn, H. Pan, B. Woods, T. D. Stanescu, and S. Das Sarma, Estimating disorder and its adverse effects in semiconductor Majorana nanowires, *Physical Review Materials* **5**, 124602 (2021), arXiv:2109.00007.
- [22] P. Yu, B. D. Woods, J. Chen, G. Badawy, E. P. A. M. Bakkers, T. D. Stanescu, and S. M. Frolov, Delocalized states in three-terminal superconductor-semiconductor nanowire devices, *SciPost Phys.* **15**, 005 (2023).
- [23] T. D. Stanescu, R. M. Lutchyn, and S. Das Sarma, Majorana fermions in semiconductor nanowires, *Phys. Rev. B* **84**, 144522 (2011).
- [24] M. Pendharkar, B. Zhang, H. Wu, A. Zarassi, P. Zhang, C. P. Dempsey, J. S. Lee, S. D. Harrington, G. Badawy, S. Gazibegovic, R. L. M. O. het Veld, M. Rossi, J. Jung, A.-H. Chen, M. A. Verheijen, M. Hocevar, E. P. A. M. Bakkers, C. J. Palmstrøm, and S. M. Frolov, Parity-preserving and magnetic field-resilient superconductivity in insb nanowires with sn shells, *Science* **372**, 508 (2021).
- [25] T. Kanne, M. Marnauza, D. Olsteins, D. J. Carrad, J. E. Sestoft, J. de Bruijckere, L. Zeng, E. Johnson, E. Olsson, K. Grove-Rasmussen, and J. Nygård, Epitaxial pb on inas nanowires for quantum devices, *Nature Nanotechnology* **16**, 776 (2021).
- [26] T. Laeven, B. Nijholt, M. Wimmer, and A. R. Akhmerov, Enhanced proximity effect in zigzag-shaped Majorana Josephson junctions, *Phys. Rev. Lett.* **125**, 086802 (2020).
- [27] P. P. Paudel, T. Cole, B. D. Woods, and T. D. Stanescu, Enhanced topological superconductivity in spatially modulated planar Josephson junctions, *Physical Review B* **104**, 155428 (2021), 2106.05302v1 [cond-mat.mes-hall].
- [28] W. Mayer, J. Yuan, K. S. Wickramasinghe, T. Nguyen, M. C. Dartiailh, and J. Shabani, Superconducting proximity effect in epitaxial al-InAs heterostructures, *Applied Physics Letters* **114**, 103104 (2019).
- [29] M. Kjaergaard, H. Suominen, M. Nowak, A. Akhmerov, J. Shabani, C. Palmstrøm, F. Nichele, and C. Marcus, Transparent Semiconductor-Superconductor Interface and Induced Gap in an Epitaxial Heterostructure Josephson Junction, *Physical Review Applied* **7**, 034029 (2017).
- [30] M. C. Dartiailh, J. J. Cuzzo, B. H. Elfeky, W. Mayer, J. Yuan, K. S. Wickramasinghe, E. Rossi, and J. Shabani, Missing shapiro steps in topologically trivial Josephson junction on InAs quantum well, *Nature Communications* **12**, 78 (2021).
- [31] B. H. Elfeky, J. J. Cuzzo, N. Lotfizadeh, W. F. Schiela, S. M. Farzaneh, W. M. Strickland, D. Langone, E. Rossi, and J. Shabani, Evolution of 4π -Periodic Supercurrent in the Presence of an In-Plane Magnetic Field, *ACS Nano* **17**, 4650 (2023).
- [32] W. Mayer, M. C. Dartiailh, J. Yuan, K. S. Wickramasinghe, E. Rossi, and J. Shabani, Gate controlled anomalous phase shift in al/InAs Josephson junctions, *Nature Communications* **11**, 212 (2020).
- [33] C. W. Groth, M. Wimmer, A. R. Akhmerov, and X. Waintal, Kwant: A software package for quantum

transport, [New Journal of Physics](#) **16**, 063065 (2014).

- [34] C. W. J. Beenakker, Three “universal” mesoscopic josephson effects, in *Transport Phenomena in Mesoscopic Systems*, edited by H. Fukuyama and T. Ando (Springer Berlin Heidelberg, Berlin, Heidelberg, 1992) pp. 235–253.
- [35] In reality, the magnetic field will also suppress the superconducting gap, however, for the magnetic field considered, such effect is much smaller than the one arising from the reduction of the decay length of the ABS states.
- [36] The qualitative picture is always the same as long as g_{sc} doesn't vanish, independent of the detailed value.

SUPPLEMENTARY INFORMATION

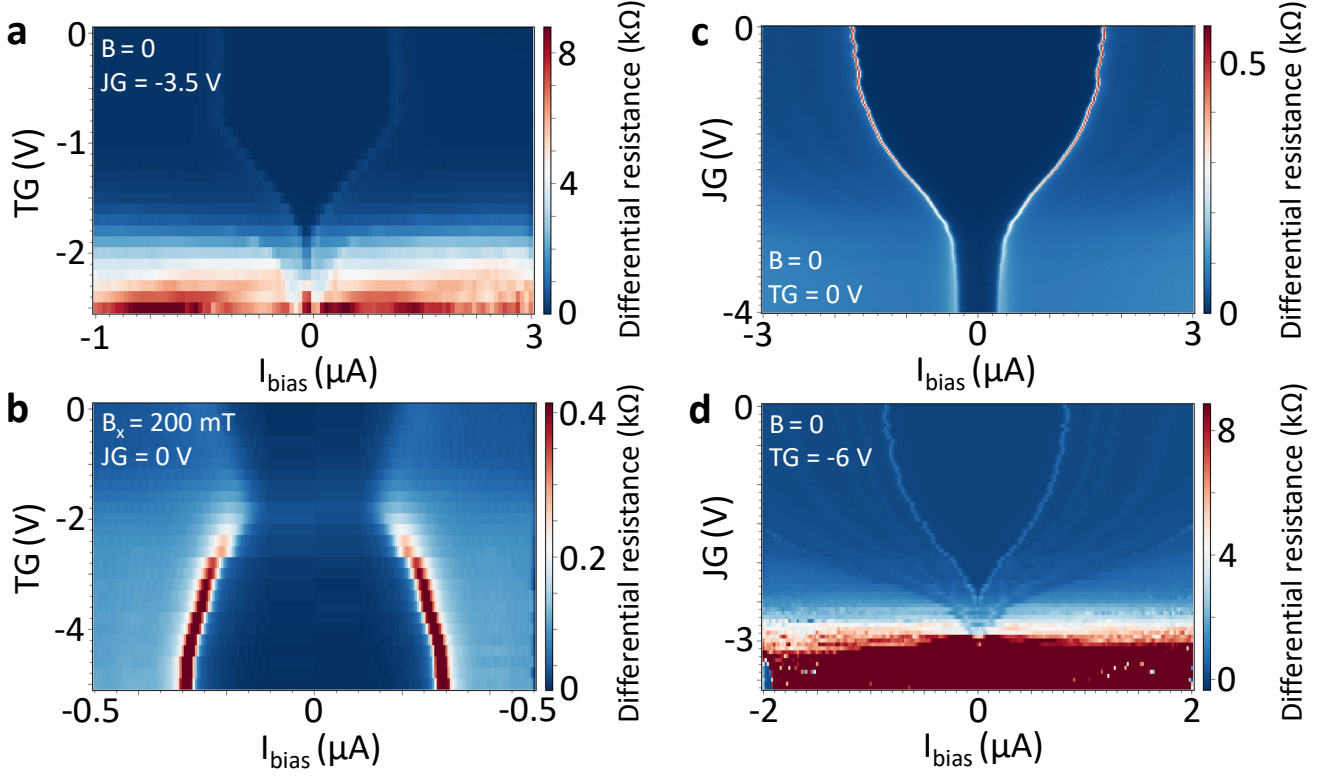


FIG. S1. **Supercurrent gate dependence at zero field and in-plane fields parallel to the supercurrent.** (a) Differential resistance as a function of bias current and TG voltage at zero field and $JG = -3.5$ V. (c) Differential resistance as a function of bias current and JG voltage at zero field and $TG = 0$ V. JG can not fully pinch off the supercurrent since it doesn't cover the ends of the junction and supercurrent can flow across the junction there. (d) Differential resistance as a function of bias current and TG voltage at zero field and $TG = -6$ V. JG can fully pinch off the supercurrent when the ends of the junction are depleted by the TG. (b) Differential resistance as a function of bias current and TG voltage at $B_x = 200$ mT and $JG = 0$, supercurrent is enhanced when TG is below -2 V.

THEORETICAL ANALYSIS

Simulation details— In the simulations, The system sizes and the superconducting gap are rescaled for the sake of numerical efficiency, while maintaining a proper ratio between the coherence length and the relevant lengths. The resulting superconducting gap $\Delta = 0.8\mu$ where μ is the Fermi energy used in the normal strip and the superconductors. The implemented Hamiltonian in the tight-binding model is the following for the normal metal (orange strip):

$$\begin{aligned}
 H_N = \sum_{i,j,\alpha,\beta} & [(4t - \mu)\tau_{z0} + E_Z \tau_{0y}]_{\alpha,\beta} c_{i,j,\alpha}^\dagger c_{i,j,\beta} + \left\{ [-t\tau_{z0} - i l_{soc}\tau_{zy}]_{\alpha,\beta} c_{i,j,\alpha}^\dagger c_{i,j+1,\beta} \right. \\
 & \left. + [-t\tau_{z0} + i l_{soc}\tau_{zx}]_{\alpha,\beta} c_{i,j,\alpha}^\dagger c_{i+1,j,\beta} + h.c. \right\}
 \end{aligned} \tag{1}$$

in the Nambu spinor basis. Here the position of the lattice is $(x, y) = (j, i)a$, a is the lattice constant, $\alpha, \beta = 1 - 4$ denote the spin and electron/hole degrees of freedom. $\tau_{m,n}$ means σ_m operator in the electron/hole sector, and σ_n in the spin degree of freedom, where σ_0 is the identity matrix and $\sigma_{x,y,z}$ is the usual Pauli matrix. The tunneling parameter t is $\hbar^2/2m^*a^2$, m^* is the effective mass, a is the lattice constant, $l_{soc} = \alpha_{soc}/2a$, α_{soc} is the Rashba SOC

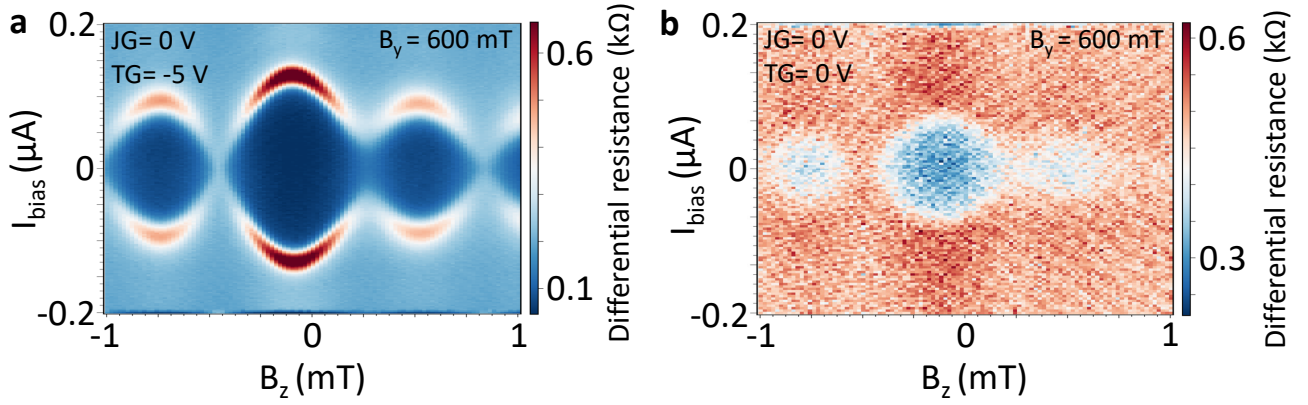


FIG. S2. **Fraunhofer patterns at high fields.** (a) Differential resistance as a function of bias current and B_z at $B_y = 600$ mT and $TG = -5$ V. Supercurrent in the main lobe shows around 50Ω resistance. (b) Differential resistance as a function of bias current and B_z at $B_y = 600$ mT and $TG = 0$ V. Fraunhofer patterns shows significant finite resistance.

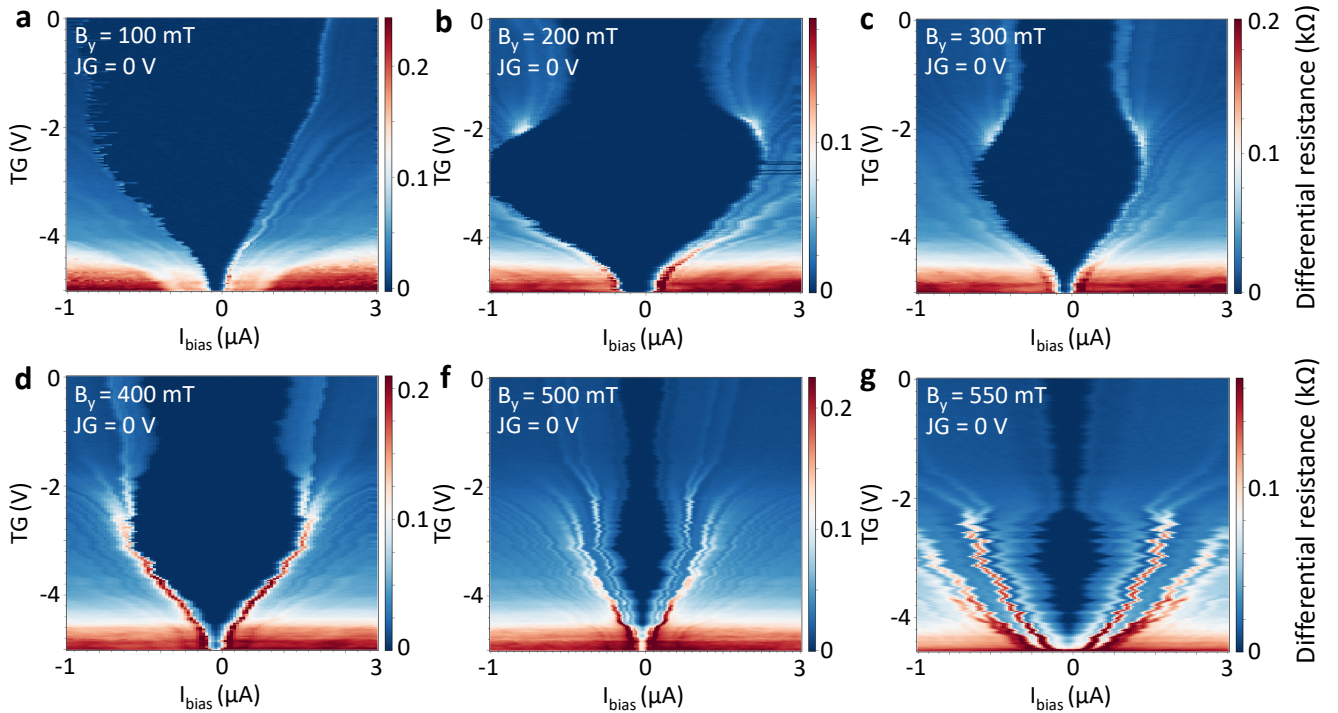


FIG. S3. **Enhancement of supercurrent at finite fields in another device.** In device B with the same geometry, enhanced supercurrent can be observed at finite fields when TG depletes ($TG < -2$ V) the 2DEG in the holes (b-g). In this device, JG is misaligned with the junction so TG can also tune the chemical potential in the junction and fully deplete the supercurrent.

strength. E_Z represents the Zeeman term when we apply a magnetic field along the y direction. In our simulations, $t = 7.32\Delta$, $l_{soc} = 0.23\Delta$. In the depleted region (green), we have

$$\begin{aligned}
 H_h = \sum_{i,j,\alpha,\beta} & [(4t - \mu_h)\tau_{z0} + E_Z \tau_{0y}]_{\alpha,\beta} c_{i,j,\alpha}^\dagger c_{i,j,\beta} + \left\{ [-t\tau_{z0} - i l_{soc}\tau_{zy}]_{\alpha,\beta} c_{i,j,\alpha}^\dagger c_{i,j+1,\beta} \right. \\
 & \left. + [-t\tau_{z0} + i l_{soc}\tau_{zx}]_{\alpha,\beta} c_{i,j,\alpha}^\dagger c_{i+1,j,\beta} + h.c. \right\}
 \end{aligned} \quad (2)$$

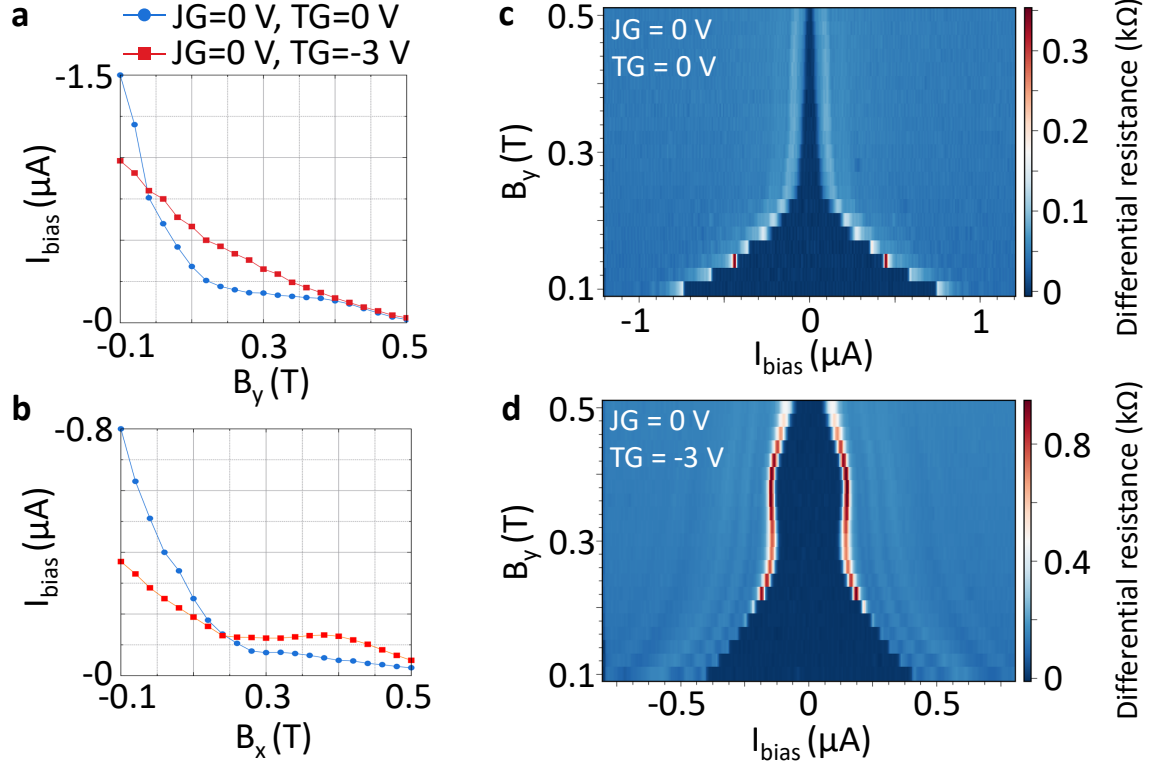


FIG. S4. **Supercurrent in-plane field dependence for different gate configurations in device B.** (a) Switching current as functions of B_y for depleted holes and non-depleted holes. (b) Switching current as functions of B_x for depleted holes and non-depleted holes. (c) Differential resistance as functions of bias current and B_y for non-depleted holes. (d) Differential resistance as functions of bias current and B_y for depleted holes.

with a different chemical potential μ_h . And in the superconductor, the Hamiltonian is

$$\begin{aligned}
 H_S = \sum_{i,j,\alpha,\beta} & [(4t - \mu)\tau_{z0} + g_{sc} E_Z \tau_{0y} + \Delta(\cos \phi \tau_{x0} - \sin \phi \tau_{y0})]_{\alpha,\beta} c_{i,j,\alpha}^\dagger c_{i,j,\beta} \\
 & + \left\{ [-t \tau_{z0} - i l_{soc} \tau_{zy}]_{\alpha,\beta} c_{i,j,\alpha}^\dagger c_{i,j+1,\beta} + [-t \tau_{z0} + i l_{soc} \tau_{zx}]_{\alpha,\beta} c_{i,j,\alpha}^\dagger c_{i+1,j,\beta} + h.c. \right\}
 \end{aligned} \tag{3}$$

where the phase of the pairing gap Δ is $\phi = -\varphi/2$ in superconductors to left of the normal strip, and $\varphi/2$ on the right. g_{sc} represents the ratio between the g -factor in superconductors and that of the normal metal. Here We choose $g_{sc} = 1/2$ in the simulations [36]. In the punched hole setup, in the unit of coherence length ξ , the system sizes are $L_x = 0.5, L_{h,1} = 0.17, L_{h,2} = 1.67, L_h = 3, L_{x,l} = 4.67, L_{y,l} = 9.5, L_y = 19.17$. The hole has a horizontal width $L_{x,h} = 0.5$ and a vertical width $L_{y,h} = 1.17$. In the two-strip setup, the parameters are $l_1 = l_3 = 0.5/\xi, l_s = 7.17\xi, l_w = 1.83\xi$

Numerical results.—From numerical simulations, see Fig. S5, we observe that in the punched hole structure, the SOC strength and the direction of the magnetic field don't alter the qualitative trend. So it is justified that we use zero SOC for simplicity. In the simplified two-strip structure, we see that the general trend can be well captured by the first energy band, see Fig. S6. Therefore, we can shrink the width in the y -direction and focus only on the single subband case.

Now to understand the dependence of the supercurrent on the two-strip distance in the simplified structure (see Fig. 6(b) and (c)), we calculate the reflection matrix at the interface between the middle superconductor and the right normal strip. The property of this interface is important since the phase jump φ is across the normal strip. To do this, we leave out the right superconductor, and make the normal strip and the left superconductor semi-infinite, see the schematic in Fig. S7(a). The incoming electron mode (denoted by black arrow) is assumed to have amplitude one, and we assume the outgoing wavefunction consists of electron mode (denoted by right-pointing black arrow) and

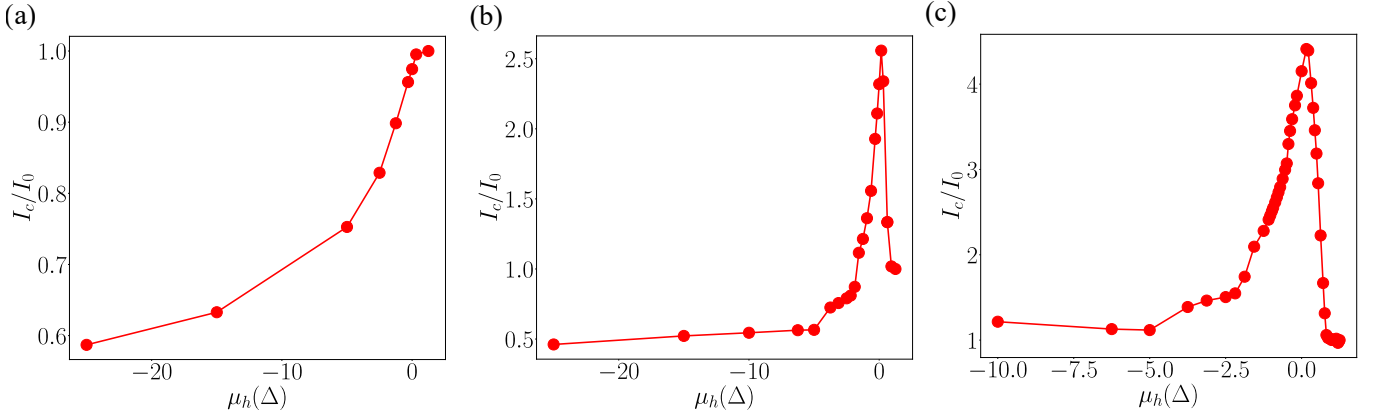


FIG. S5. Comparison of current behavior at different parameters. (a) Supercurrent vs depletion potential at $E_z = 0$ without SOC in the punched-hole setup. (b). Supercurrent vs depletion potential at $E_z = 1.14\Delta$ without SOC in the punched-hole setup. (c) Supercurrent vs depletion potential at $E_z = 1.14\Delta$ when the magnetic field is along the x -direction with SOC in the punched-hole setup.

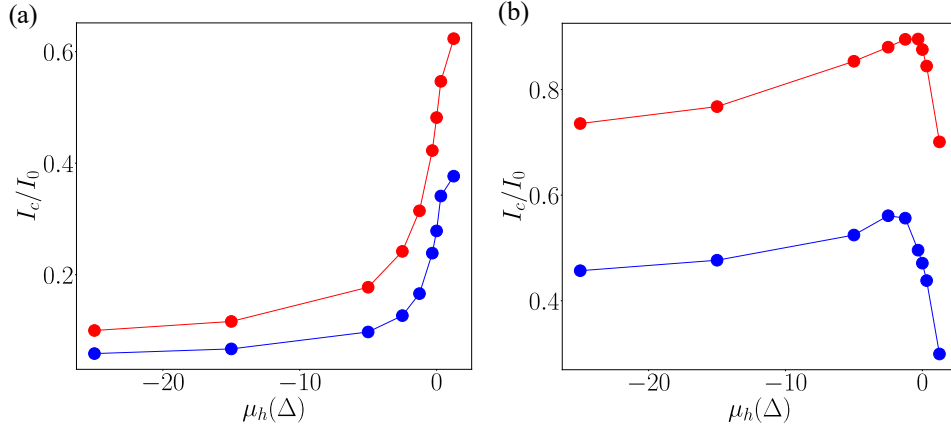


FIG. S6. Critical current I_c from the first band (red) and the rest bands (blue) in the simplified setup. (a) I_c dependence on the chemical potential of the green strip μ_h at $l_2 = \xi/6$. I_c is scaled by the total critical current without depletion. (b) Scaled I_c dependence on μ_h at $l_2 = \xi/2$.

hole mode (right-pointing white arrow). Their amplitudes then give the normal reflection r_N and Andreev reflection r_A coefficients, respectively. We then solve the wavefunction over the entire region by continuity equations.

Since we are studying the case without magnetic field or SOC, we assume the entire wavefunction is in the same spin configuration. The wavefunction is then reduced to two degrees of freedom (electron and hole). In the right normal metal, the wavefunction is

$$\psi = (1, 0)e^{-ik_e x} + r_N(1, 0)e^{ik_e x} + r_A\sqrt{k_e/k_h}(0, 1)e^{-ik_h x} \quad (4)$$

where r_N is the normal reflection coefficient, and r_A is the Andreev reflection amplitude. The electron/hole wavevector is given by $k_{e,h} = \sqrt{2m^*(\mu \pm E)/\hbar^2}$. For the middle superconducting strip, its finite width allows overlap of four modes (decaying in different directions):

$$\begin{aligned} \psi = & C_1(1, e^{i\theta})e^{\lambda x + ik_s x} + C_2(1, e^{-i\theta})e^{\lambda x - ik_s x} \\ & + C_3(1, e^{-i\theta})e^{-\lambda x + ik_s x} + C_4(1, e^{i\theta})e^{-\lambda x - ik_s x} \end{aligned} \quad (5)$$

where $\cos \theta = E/\Delta$, Δ is the superconducting gap, k_s, λ are non-negative and $k_s + i\lambda = \sqrt{2m^*(\mu + i\Delta \sin \theta)/\hbar^2}$. The wavefunction in the depleted strip (green) is

$$\begin{aligned} \psi = & D_1(1, 0)e^{ik'_c x} + D_2(1, 0)e^{-ik'_c x} \\ & + D_3(0, 1)e^{ik'_h x} + D_4(0, 1)e^{-ik'_h x} \end{aligned} \quad (6)$$

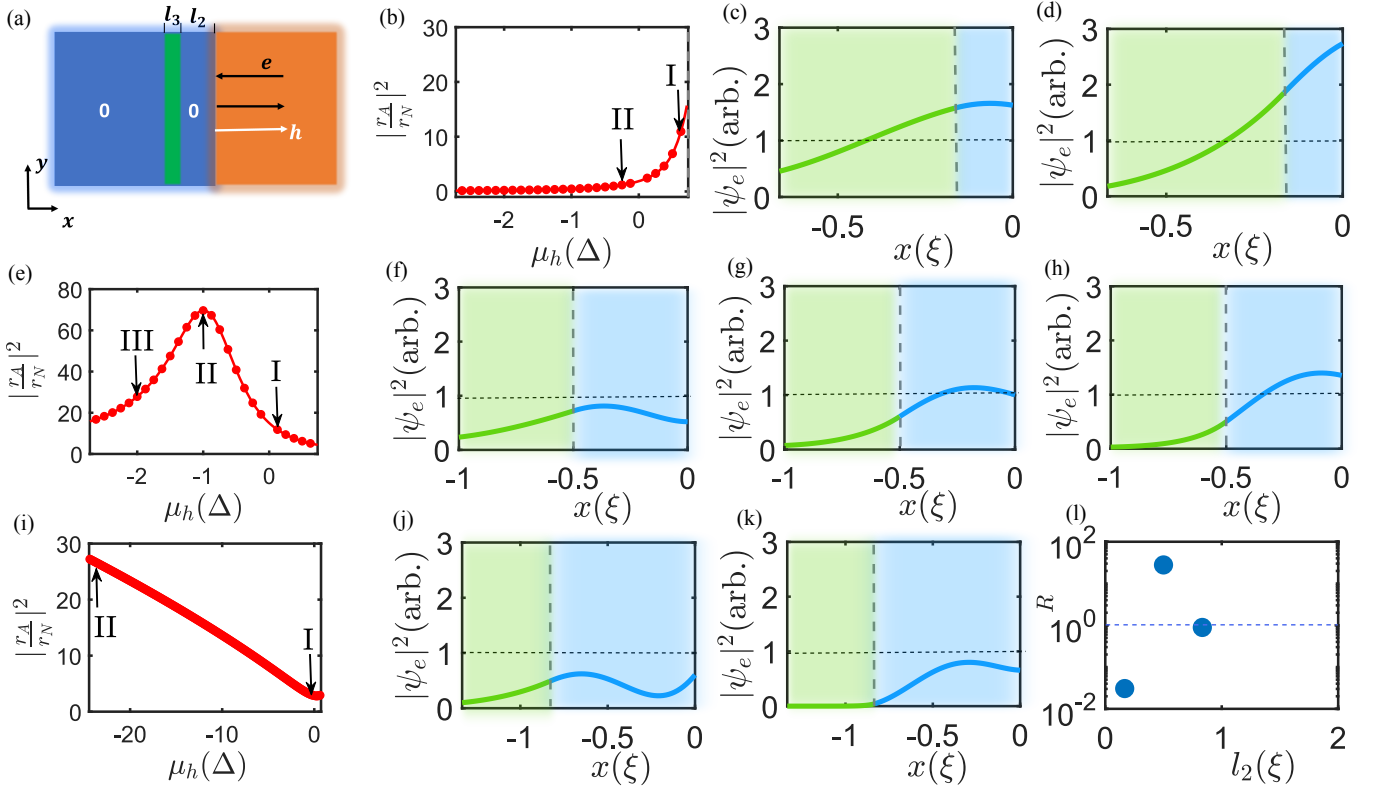


FIG. S7. Ratio of Andreev reflection r_A to normal reflection r_N as a function of l_2 between two strips calculated at energy $E = 0$. (a) Setup for calculation of the reflection matrix. The phases are assumed zero for the left and middle superconductors. Here we focus on the x -direction degree of freedom. (b) $|r_A/r_N|^2$ at $l_2 = \xi/6$. (c) Distribution of electron density in the depleted strip (green) and middle superconductor (blue) $|\psi_e(x)|^2$ at Point II in the (b) panel where the Andreev reflection is strong. (d) $|\psi_e(x)|^2$ at Point II in the (b) panel. (e) $|r_A/r_N|^2$ at $l_2 = \xi/2$. (f). $|\psi_e(x)|^2$ at Point I of the (e) panel. (g) $|\psi_e(x)|^2$ at Point II of (e) Panel. (h) $|\psi_e(x)|^2$ at Point III of (e) Panel. (i) $|r_A/r_N|^2$ at $l_2 = 5\xi/6$. Due to the large distance and weak coupling between the two strips in this case, the effect of the depletion is much weaker and therefore we examine a larger range of μ_h . (j). $|\psi_e(x)|^2$ at Point I of (i) Panel. (k) $|\psi_e(x)|^2$ at II in (i) Panel. (l) Relative Andreev reflection strength $R = |r_A/r_N|^2/R_0$ at $\mu_h = -\Delta$ as a function of strip distance l_2 . Here R_0 is the value of $|r_A/r_N|^2$ without depletion for each l_2 choice.

where the electron/hole wavevector in the depleted strip is $k'_{e,h} = \sqrt{2m^*(\mu_h \pm E)/\hbar^2}$ where μ_h is the chemical potential in the depleted strip.

In the left superconductor, things are simple. There are only two vanishing modes:

$$\psi = E_1(1, e^{i\theta})e^{\lambda x + ik_s x} + E_2(1, e^{-i\theta})e^{\lambda x - ik_s x} \quad (7)$$

By matching the boundary conditions (both wavefunction ψ and the its gradient $\partial\psi/\partial x$ are continuous) at all interfaces, we then can solve for the coefficients, achieve the reflection matrix, and reconstruct the wavefunction profile in the entire region at $E = 0$, see Fig. S7. One can see that the strength of the Andreev reflection depends on the depletion potential, in a similar manner to the supercurrent. It reveals that the supercurrent enhancement at certain depletion strength is due to the enhanced Andreev reflection at this point.

If we look at the wavefunction distribution in the depleted strip and middle superconductor, we would see that increasing the depletion strength is always pushing the particle distribution more to the right side of the middle superconductor. The Andreev reflection is always maximum when the amplitude of the electron sector (denoted as ψ_e) is close to one at the superconductor/normal interface (defined as $x = 0$ position here). When the strip distance is short, the $|\psi_e|$ is big (> 1) at the interface without depletion, so stronger depletion is adding the amplitude further, which then decrease $|r_A|$. When the strip distance is increased, there is more space in the middle superconductor, and the electrons spread more towards the left side. The amplitude at $x = 0$ is small without depletion. Now, at a proper depletion, the amplitude gets close to one and $|r_A|$ is optimal. At even larger strip distance, the depletion potential needs to be stronger to increase the electron amplitude at $x = 0$. Therefore, within our parameter range of μ_h , $|r_A|$ is increasing with stronger depletion.

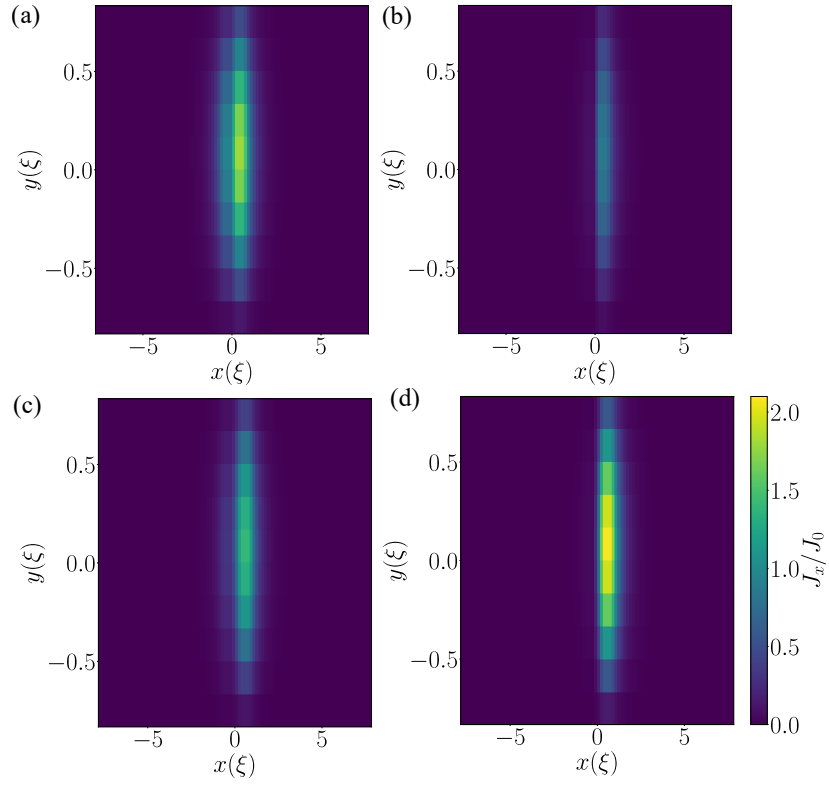


FIG. S8. Distribution of the x - direction current density $J_x(x, y)$ in the two-strip setup. The density is scaled by J_0 which is the average supercurrent density without depletion at $l_2 = \xi/6$. (a) $l_2 = \xi/6$, no depletion. (b) $l_2 = \xi/6, \mu = -1.25\Delta$. (c) $l_2 = \xi/2$, no depletion. (d) $l_2 = \xi/2, \mu_h = -1.25\Delta$. All plots share the same color bar.

So far we have clarified the picture behind the intriguing current behavior as a function of strip distance or magnetic field. Now we look at the spatial distribution of the current. We present results at $l_2 = \xi/6, \xi/2$ without magnetic field in Fig. S8.